

This work was written as part of one of the author's official duties as an Employee of the United States Government and is therefore a work of the United States Government. In accordance with 17 U.S.C. 105, no copyright protection is available for such works under U.S. Law. Access to this work was provided by the University of Maryland, Baltimore County (UMBC) ScholarWorks@UMBC digital repository on the Maryland Shared Open Access (MD-SOAR) platform.

Please provide feedback

Please support the ScholarWorks@UMBC repository by emailing scholarworks-group@umbc.edu and telling us what having access to this work means to you and why it's important to you. Thank you.

Ultrafast Carrier Dynamics of Monolayer WS₂ via Broad-Band Time-Resolved Terahertz Spectroscopy

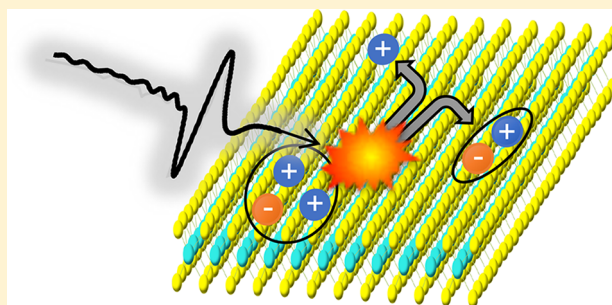
Jon K. Gustafson,^{*,†} Paul D. Cunningham,[‡] Kathleen M. McCreary,[‡] Berend T. Jonker,[‡] and L. Michael Hayden^{*,†}

[†]Department of Physics, UMBC, 1000 Hilltop Circle, Baltimore, Maryland 21250, United States

[‡]U.S. Naval Research Laboratory, Washington, District of Columbia 20375, United States

S Supporting Information

ABSTRACT: We report on the ultrafast carrier dynamics of monolayer WS₂ using broad-band time-resolved terahertz spectroscopy (TRTS). We find that upon photoexcitation, there is an increase in the conductivity. We attribute this photoinduced increase in conductivity to ultrafast positive trion formation. Trion formation in two-dimensional materials is a consequence of the enhanced Coulombic interactions between electrons and holes. We find that trions in monolayer WS₂ contribute to the photoconductivity in three ways: a Drude response, a broad resonance response, and a dissociation response at the trion binding energy. This is the first direct measurement of the trion binding energy in the far-infrared. Our results provide a comprehensive understanding of how trions behave in two-dimensional systems and should be broadly useful in studying the carrier dynamics of other two-dimensional systems.



INTRODUCTION

Atomically thin transition metal dichalcogenides (TMDs), such as WS₂, WSe₂, MoS₂, and MoSe₂, are a class of two-dimensional materials that have attracted much attention in the past decade. Unlike graphene, TMDs are true two-dimensional semiconductors in the sense that they have a significant band gap.¹ In the monolayer limit, TMDs are direct band-gap materials that exhibit strong photoluminescence² and show promise for next-generation optoelectronic devices.^{3–5} Monolayer TMDs also have strong potential for quantum computing applications as they have valley-dependent optical properties that result from spin-valley locking.^{5–10}

One of the most unique properties of monolayer TMDs is the existence of tightly bound excitons with binding energies on the order of several hundred millielectronvolts.^{11,12} These excitons are a consequence of quantum confinement and reduced dielectric screening that enhances the Coulombic interactions between electrons and holes.¹³ The strong Coulombic interactions in TMDs are sufficient to support charged exciton (i.e., trion) formation as well. A trion is a bound, three-body quasi-particle state that forms when an exciton captures either an additional hole (positive trion) or an additional electron (negative trion). In monolayer TMDs, trions have been predicted^{14,15} and observed^{16–24} to have binding energies of approximately 25–40 meV. Trions, in TMDs, have a number of technologically interesting properties. For example, in WS₂, trions have been shown to induce band-gap renormalization through Coulombic screening,²⁵ which is important for optoelectronic applications. Addition-

ally, trions in WS₂ have been observed to have a higher valley-polarized emission,²⁶ which is potentially important in the emerging field of valleytronics. Trions in WS₂ have also been shown to be sensitive to molecular adsorption,¹⁹ which could find applications in chemical sensing. Therefore, as researchers look to fabricate devices out of TMD materials, it is clear that a fundamental understanding of the behavior of trions in these two-dimensional systems is necessary.

Previous photophysical studies of TMDs have primarily utilized time-resolved photoluminescence, transient absorption, and optical pump–probe spectroscopy in order to study the ultrafast excited state dynamics. These studies have generally observed charge carrier dynamics on two distinct time scales: a fast, picosecond decay assigned to carrier cooling^{27,28} and carrier trapping²⁹ followed by a slow, tens of picoseconds decay attributed to interband recombination,³⁰ exciton recombination,³¹ exciton–exciton annihilation,^{32,33} exciton–phonon scattering,³⁴ and trion trapping.³⁵ These studies were not able to directly probe the conductivity of TMDs though, which is crucial for device realization. Time-resolved terahertz (THz) spectroscopy (TRTS) however is a powerful tool that can probe conductive species in materials, in an all-optical, noncontact fashion. One of the main advantages that TRTS presents over other complementary techniques is

Received: September 5, 2019

Revised: November 20, 2019

Published: November 20, 2019

its ability to discriminate between different kinds of charge carriers with subpicosecond resolution.

A few groups have studied the carrier dynamics of TMDs with TRTS;^{29,35–38} however, there is still a lack of agreement in the literature on the underlying physics that governs the behavior of charge carriers in TMDs in the terahertz spectral regime. One reason for this disagreement is because frequency-dependent photoconductivity measurements in TRTS studies are typically made in a narrow frequency band in which many different conductivity models look very similar. For example, in monolayer MoS₂, Docherty et al. describe the photoconductivity as a Drude response combined with two stronger Lorentzian responses,²⁹ whereas Cunningham et al. describe the photoconductivity via the Drude–Smith model.³⁷ While these two models both fit the measured photoconductivity in MoS₂ relatively well in the 0–2 THz frequency range, they are based on different underlying physics and thus provide different interpretations on how charge carriers behave in TMDs. Broad-band TRTS however may allow for differences between conductivity models to be identified.

In this paper, we study the dominant contributions to the photoconductivity in chemical vapor deposition (CVD) grown monolayer WS₂ via broad-band TRTS, which has not been done to the best of our knowledge. In our broad-band TRTS setup, we are sensitive to charge carriers that have a conductivity response in the 0.5–8 THz frequency range. Due to our broader bandwidth, we observed several distinct features in the photoconductivity spectrum of monolayer WS₂, and as a result, we were able to model the photoconductivity effectively. From the model, we report that positive trions play a dominant role in determining the conductivity of monolayer WS₂. Specifically, we find that (1) the photoinduced increase in conductivity is due to defect-mediated positive trion formation, (2) the overall photoconductivity is well modeled by a Drude component, a broad resonance due to the effects of charge buildup at grain boundaries, and a component due to trion dissociation, which allows us to (3) make the first far-infrared direct measurement of the trion binding energy.

EXPERIMENTAL METHODS

Sample Preparation. Monolayer WS₂ films were prepared via chemical vapor deposition (CVD). One film we acquired commercially from 2D Semiconductors, in which the monolayer WS₂ film was grown on sapphire and then transferred to a TOPAS (cyclic olefin copolymer) substrate. The other film we synthesized at the Naval Research Laboratory (NRL). Synthesis of this monolayer WS₂ film was performed at ambient pressure in a 2 in. diameter quartz tube furnace on SiO₂/Si substrates (275 nm thickness of SiO₂).³⁹ Prior to use, all SiO₂/Si substrates were cleaned in acetone, IPA, and Piranha etch and then thoroughly rinsed in DI water. At the center of the furnace we positioned a quartz boat containing ~1 g of WO₃ powder. Two SiO₂/Si wafers were positioned face-down, directly above the oxide precursor. A separate quartz boat containing sulfur powder was placed upstream, outside the furnace-heating zone. The upstream SiO₂/Si wafer contained perylene-3,4,9,10-tetracarboxylic acid tetrapotassium salt (PTAS) seeding molecules, while the downstream substrate was untreated. The hexagonal PTAS molecules were carried downstream to the untreated substrate and promoted lateral growth of the monolayer WS₂. Pure argon (65 sccm) was used as the furnace heated to the target temperature. Upon reaching the target temperature of 825 °C,

10 sccm H₂ was added to the Ar flow and maintained throughout the 10 min soak and subsequent cooling. A thin layer of poly(methyl methacrylate) (PMMA) was spun onto the surface of the entire growth substrate and then submerged in buffered oxide etchant. After several hours the oxide layer was removed, freeing the WS₂/PMMA film from the growth substrate. The sample was subsequently transferred to H₂O to rinse chemical etchants, where a TOPAS substrate was used to lift the film out of the water. A 2000 rpm spin and subsequent 150 °C bake in ambient conditions improved the uniformity and adhesion to the substrate, after which the PMMA was dissolved in acetone.⁴⁰

Time-Resolved Terahertz Spectroscopy. An optical-pump terahertz-probe spectrometer was used to measure the photoconductivity of our monolayer WS₂ films. The details of how the photoconductivity is measured as well as how the photoconductivity is extracted from the raw data has been described previously.⁴¹ Our TRTS setup³⁷ is based on a regeneratively amplified Ti:sapphire laser (Coherent Legend Elite Duo) which generates 30 fs pulses of 800 nm light at a 1 kHz repetition rate. About one-half of the output is used to pump an optical parametric amplifier (Coherent OperA Solo), which allows for tunable excitation pulses. The other half is dedicated to terahertz generation and terahertz detection. To generate broad-band terahertz pulses, we employ a two-color, air-plasma technique in which we focus the 800 nm light through a BBO crystal and mix the fundamental and second harmonic in a laser-induced air-plasma filament.⁴² To detect terahertz pulses, we use electro-optic sampling in a 300 μm thick GaP crystal, which provides a continuous bandwidth from 0.5 to 8 THz^{43,44} (see [Supporting Information](#)). The terahertz beam diameter is ~800 μm, which is smaller than the 2 mm excitation beam. The entire terahertz beam path is purged with dry air to avoid water vapor absorption. All measurements reported in this work were performed in vacuum (<5 mTorr). In addition, a closed cycle refrigerator (CCR) system (with temperature control from 20 to 300 K) was used for temperature-dependent photoconductivity measurements.

RESULTS AND DISCUSSION

Figure 1a shows the room-temperature ultraviolet–visible (UV–vis) absorption spectra of the two monolayer WS₂ films we studied: the commercial film acquired from 2D Semiconductors and the film we synthesized at the Naval Research Laboratory (NRL). Similar to others,³⁶ we observe three distinct resonances in the absorption spectrum of monolayer WS₂, which correspond to the A, B, and C excitons. In the commercial sample, the A, B, and C exciton peaks are located at 2.02 (614 nm), 2.42 (512 nm), and 2.88 eV (430 nm), respectively. In the NRL sample, the A, B, and C exciton peaks are located at 2.07 (600 nm), 2.45 (507 nm), and 2.88 eV (430 nm), respectively. We attribute the differences in exciton peak positions and amplitudes between the two samples to differences in sample fabrication and transfer to our TOPAS substrates.

To investigate the dynamics of the photoinduced conductivity of monolayer WS₂, we used time-resolved terahertz spectroscopy (TRTS). The terahertz photoconductivity dynamics were found by measuring the fractional change in transmission of the peak of the terahertz waveform as a function of time after pump excitation. Given that the trion binding energy in monolayer WS₂ is close to room temper-

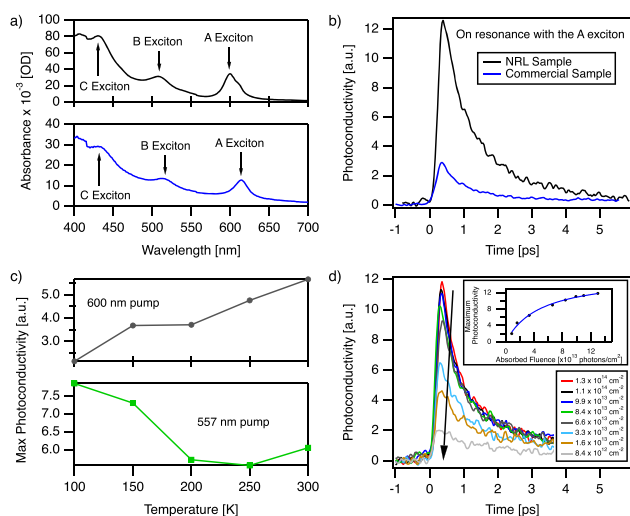


Figure 1. (a) Ultraviolet–visible (UV–vis) absorbance of monolayer WS_2 on TOPAS at room temperature for the NRL (black) and commercial (blue) films. Peaks A, B, and C denote the different exciton resonances. (b) Terahertz photoconductivity dynamics of monolayer WS_2 as a function of time after photoexcitation at 20 K (incident fluence $\approx 7.0 \times 10^{14}$ photons/cm 2) for the NRL (black) and commercial (blue) films. (c) Maximum value of the terahertz photoconductivity of the NRL monolayer as a function of temperature. As the temperature is lowered from room temperature, the photoconductivity due to excitation at the room temperature resonance of 600 nm (gray circles) decreases. When exciting at the 20 K resonance of 557 nm (green squares), the conductivity rises as the temperature is lowered. [Supporting Information](#) shows the evolution of the A exciton as a function of temperature. (d) Terahertz photoconductivity dynamics of monolayer WS_2 (NRL film) at various absorbed fluences when pumping on resonance with the A exciton at 20 K. (Inset) Plot of the maximum photoconductivity as a function of absorbed fluence. Solid blue line is a fit to the data with a saturable absorber model (eq 1).

ature, we chose to perform experiments at 20 K in order to mitigate any temperature effects on measuring the trion dissociation. For resonant excitation at 20 K, the commercial sample was pumped at 584 nm and the NRL sample at 557 nm (see [Supporting Information](#) for a discussion on the temperature dependence of the absorption spectrum). Similar to TRTS studies in other TMDs,^{29,36,37} we observed a photo-induced increase in conductivity in monolayer WS_2 (Figure 1b). We attribute this increase in conductivity to ultrafast positive trion formation.

In order to understand trions as the source of positive photoconductivity in monolayer WS_2 , we first consider the role excitons play in this system. Being charge neutral, excitons do not interact with terahertz radiation in the same way that free charge carriers do. Free charge carriers absorb terahertz radiation via intraband transitions, resulting in Drude-like responses. Excitons on the other hand, being hydrogen-like systems, absorb/emit terahertz radiation in determined quantized energies, resulting in resonance-like responses. In WS_2 , the exciton binding energy is on the order of several hundred millielectronvolts (around 100 THz) and the 1s–2p transition has an energy over 100 meV (around 24 THz).¹² Thus, there should be resonances in the photoconductivity at these energies; however, given our system bandwidth of 0.5–8 THz, we do not expect to see direct, spectroscopic evidence of excitons.

Given that we do not expect to see direct, spectroscopic evidence of excitons, the observed positive photoconductivity in monolayer WS_2 is surprising because pumping on resonance with the A exciton at our moderate fluences should only create excitons in the system. The positive photoconductivity must then arise from some other source. Since defects are expected to have an impact on the terahertz conductivity in TMDs, we must consider the role that defects may play in the system. In monolayer WS_2 , sulfur vacancies, the most common type of defect in CVD-grown WS_2 ,⁴⁵ have been shown to produce states within the band gap that are close to the valence band maximum.⁴⁶ We propose that electrons in the valence band are photoexcited into these trap states by the subgap energy supplied by the pump beam, which, as a result, creates free holes in the valence band. Therefore, in addition to the photogenerated exciton population, there is initially a population of trapped electrons in defect states and a population of free holes in the valence band. We argue that the excitons then capture these free holes almost immediately to form three-body, bound quasiparticles (positive trions) so that by the time the terahertz photoconductivity reaches a maximum, the photoconductivity is completely determined by the behavior of the trions, excitons, and trapped electrons. Excitons, however, as mentioned previously, do not interact strongly with the terahertz radiation in our frequency window and thus should not contribute strongly to the photoconductivity. The electrons trapped in defect states should not contribute to the photoconductivity either, since they are immobile. Therefore, the observed increase in photoconductivity must arise from trions.

In the mechanism described above, we suggest that excitons and holes form positive trions almost immediately, thus making trions the source of positive photoconductivity. One may also propose however that ultrafast trion formation does not occur and that the source of positive photoconductivity is actually due to the free holes that were created by photoexciting valence band electrons into the defect states. To verify that ultrafast trion formation truly occurs and that the observed increase in terahertz photoconductivity is not just due to holes, we looked at the maximum value of the terahertz photoconductivity as a function of temperature at fixed wavelengths. We find that when pumping the NRL monolayer at 600 nm, which is resonant with the A exciton at room temperature, the maximum value of the terahertz photoconductivity decreases as the temperature is lowered. When pumping at 557 nm, which is resonant with the A exciton at 20 K, the photoconductivity rises as the temperature is lowered. This behavior (shown in Figure 1c) is in agreement with the shift in the position of the A exciton (see [Supporting Information](#)). We would not expect to see the photoconductivity track the shifting of the exciton resonance if holes were the source of the positive photoconductivity. If trions, however, were the source of positive photoconductivity, the fact that the photoconductivity tracks with the shifting of the A exciton resonance with temperature supports our model. The [Supporting Information](#) contains UV–vis absorption data as a function of temperature and shows that the A exciton blue shifts with decreasing temperature. This blue shift means that when exciting WS_2 at 600 nm (557 nm), fewer (more) excitons are formed as the temperature cools down since the energy of the A exciton shifts away from (toward) the 600 nm (557 nm) pump. Figure 1c therefore tells us that the terahertz photoconductivity decreases (increases) when fewer (more)

excitons are formed, suggesting that the terahertz photoconductivity is directly linked to exciton formation. Given that we do not expect excitons to directly contribute to the photoconductivity, trion formation must then be responsible for the increase in photoconductivity because trions are formed from excitons.

To confirm that trion formation is indeed mediated through a defect-driven process, we looked at the terahertz photoconductivity as a function of fluence (Figure 1d). As shown in the inset of Figure 1d, the maximum value of the terahertz photoconductivity saturates as the absorbed fluence increases from 8.4×10^{12} to 1.3×10^{14} photons/cm². This behavior is indicative of a defect-mediated process. As the fluence approaches the density of defects, fewer and fewer defect states are available to photoexcite electrons into. As a result, fewer holes are created, thus slowing down trion formation. Since the trion concentration saturates, the terahertz photoconductivity then saturates as well. In the inset of Figure 1d, we present a fit to the fluence-dependent photoconductivity with the saturable absorber model

$$-\frac{\Delta E}{E_0} \propto \frac{n}{n + n_s} \quad (1)$$

where n is the absorbed fluence in photons/cm² and n_s is the saturation density. From the fit we estimate the saturation density to be 4.8×10^{13} photons/cm². Lui et al. report a similar saturation response in the photoconductivity of monolayer MoS₂ over the same fluence range.³⁵

The fact that trion formation in monolayer WS₂ is defect driven explains why the photoconductivity varies so much between samples (Figure 1b). The photoconductivity of the NRL sample is four times larger than the photoconductivity of the commercial sample given the same incident fluence. This difference suggests that the NRL sample has a higher defect density than the commercial sample. The difference in defect densities between samples is further evident in the room-temperature absorption spectra of the NRL and commercial samples (Figure 1a). In the NRL absorption spectrum, there is a small peak on the right shoulder of the A exciton due to trion absorption. Mak et al. observe a similar peak in the absorption spectrum of monolayer MoS₂, which they attribute to trion absorption as well.²³ In the commercial sample absorption spectrum, however, we find that no such trion peak can be resolved. This difference in the spectra is a strong indicator that the defect density of the NRL sample is larger than that of the commercial sample because defect states play a critical role in trion formation. We attribute this difference in defect density to differences in sample growth and the transferring of the films from their growth substrates to TOPAS substrates.

To further investigate the role of trions in the photoconductivity of monolayer WS₂, we measured the frequency-dependent complex photoconductivity (see the Supporting Information for details on computing the complex photoconductivity). Here, the entire fractional pump-induced modulation of the terahertz waveform was recorded instead of just at the peak. In Figure 2, we present the sheet photoconductivity of monolayer WS₂ (commercial film) measured at several different times after photoexcitation at 20 K while pumping on resonance with the A exciton. At 600 and 800 fs after photoexcitation, the photoconductivity is dominated by a sharp resonance feature around 7.6 THz. There is a nonzero real conductivity component at low

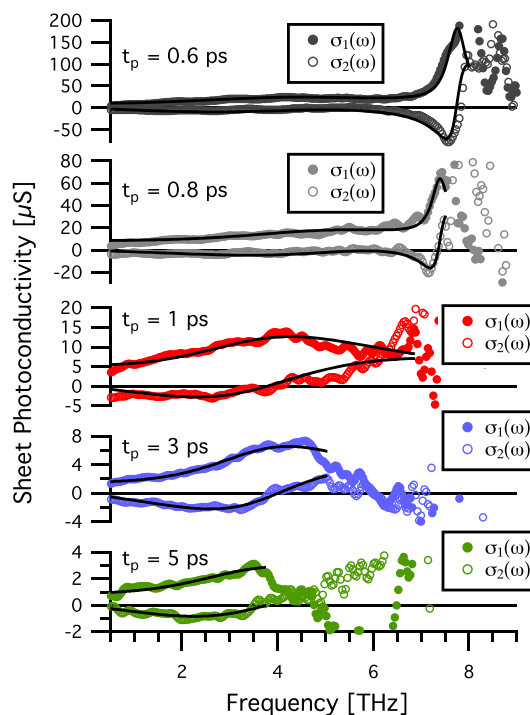


Figure 2. Complex frequency-dependent photoconductivity of monolayer WS₂ (commercial film) at 0.6, 0.8, 1, 3, and 5 ps after photoexcitation. Sample was pumped on resonance with the A exciton at 20 K (584 nm). Absorbed fluence was $\sim 1.7 \times 10^{13}$ photons/cm². Solid (open) circles are the real (imaginary) part of the induced photoconductivity. Solid lines represent fits to eq 2.

frequencies (0.5–1 THz) and a broad resonance feature around 4.4 THz as well. At 1, 3, and 5 ps after photoexcitation, the photoconductivity has decayed enough so that the signal-to-noise is decreased at the higher frequencies. For these longer delay times, the sharp resonance feature around 7.6 THz is outside the dynamic range of our system and the photoconductivity is completely described by the low-frequency component and the broad resonance feature.

In an effort to ascribe physical meaning to these conductivity features, we model the photoconductivity spectra as a sum of three oscillators. The functional form of the photoconductivity model is expressed as

$$\sigma(\omega) = \sum_{m=1}^3 \frac{iC_m\omega}{\omega^2 - \omega_{0m}^2 + i\omega\gamma_m} \quad (2)$$

where C_m is the spectral weight of the oscillator, γ_m is the line width (THz), and ω_{0m} is the resonant frequency (THz). We set the resonant frequency of the first oscillator equal to zero. By doing so, the first oscillator will reduce to the Drude model and describe the nonzero low-frequency component of the real conductivity. We place no restrictions on the two other Lorentz oscillators which describe the broad and sharp resonances in the photoconductivity.

We present the resulting fit parameters in Table 1. To extract the underlying physics from these parameters, we consider how trions interact with terahertz radiation. Being bound states, trions can dissociate if they absorb radiation of sufficient energy. In monolayer WS₂, the binding energy of the positive trion has been reported to be approximately 30 meV (7.4 THz).¹⁵ From Table 1, we see that at 600 and 800 fs after photoexcitation the resonant frequency of the third oscillator is

Table 1. Fitting Parameters for the Photoconductivity Curves in Figure 2

pump delay [ps]	C_1 [S/s]	γ_1 [THz]	ω_{01} [THz]	C_2 [S/s]	γ_2 [THz]	ω_{02} [THz]	C_3 [S/s]	γ_3 [THz]	ω_{03} [THz]
$\tau_p = 0.6$	2.8×10^8	25	0	8.2×10^8	41	4.7	4.8×10^8	3.0	7.8
$\tau_p = 0.8$	3.1×10^8	36	0	5.2×10^8	39	5.6	1.3×10^8	2.6	7.4
$\tau_p = 1.0$	1.5×10^8	27	0	3.5×10^8	35	4.5	0	0	0
$\tau_p = 3.0$	0.7×10^8	45	0	1.4×10^8	26	4.3	0	0	0
$\tau_p = 5.0$	0.4×10^8	41	0	0.6×10^8	27	4.1	0	0	0

7.8 and 7.4 THz (or 32 and 30 meV), respectively, which suggests that trion dissociation plays a significant role in determining the terahertz photoconductivity. This is the first direct measurement of the trion binding energy in the far-infrared. At 1, 3, and 5 ps after photoexcitation, we cannot extract the trion binding energy. This is because at 1, 3, and 5 ps after photoexcitation the signal-to-noise has decreased significantly at the higher frequencies and we can no longer measure the trion dissociation response.

Being *charged* quasiparticles, trions accelerate under the influence of an electric field and thus interact with terahertz radiation according to Newton's Laws. The nonzero Drude response reported in Table 1 confirms that trions exhibit a free-carrier response in the photoconductivity; however, looking at the spectral weight coefficients, we see that the strength of this Drude response is small. To understand this, we look at the effective mass of a trion. Since trions are three-body quasiparticles, they are three times as heavy as free electron/holes.^{19,35} They therefore have reduced mobility and contribute less to the conductivity.

To understand the broad resonance feature in the photoconductivity, we consider the effect of the grain boundaries on the trions. In CVD-grown monolayer WS₂, the majority of defect states are located at grain boundaries,^{47,48} which means that the majority of the trions are located at the grain boundaries as well because trion formation is a defect-mediated process. Being close to the edges, trions therefore accumulate at the grain boundaries as they are accelerated by the terahertz field. The charge buildup then in return creates a restoring force on other trions and results in a resonance-like behavior. Xing et al. observed a similar broad resonance-like behavior in the photoconductivity of multilayer WS₂; however, they argued that an exciton polarization field was responsible for the restoring force on free charge carriers, not charge buildup at grain boundaries.³⁶ This argument though cannot describe the physics of our WS₂ sample because we find that trions are the dominant species, not excitons.

In Figure 3, we present the sheet photoconductivity of monolayer WS₂ (NRL film) measured at several different absorbed fluences, again pumping on resonance with the A exciton at 20 K. Similar to before, we model the photoconductivity spectra with a three-oscillator model (eq 2). In Table 2, we report the corresponding fit parameters.

From the fit parameters, we extract the trion concentration n . To do so, we associate the parameters of our model to the physical situation using the following expression

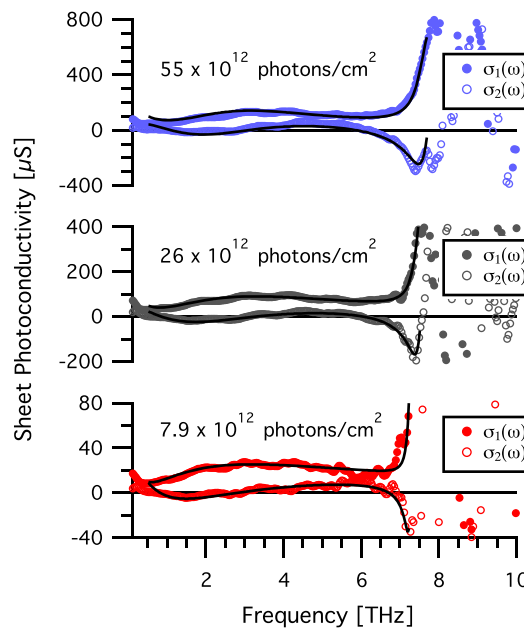


Figure 3. Complex frequency-dependent photoconductivity of monolayer WS₂ (NRL film) at various absorbed fluences. Sample was pumped on resonance with the A exciton at 20 K (557 nm). Conductivity was probed 400 fs after excitation. Solid (open) circles are the real (imaginary) part of the induced photoconductivity. Solid lines represent fits to eq 2.

$$\Delta\sigma(\omega) = \frac{n_F e^2}{m} \times \frac{i\omega}{\omega^2 + i\omega\gamma_F} + \frac{n_B e^2}{m} \times \frac{i\omega}{\omega^2 - \omega_B^2 + i\omega\gamma_B} + \frac{nfe^2}{m} \times \frac{i\omega}{\omega^2 - \omega_{Dis}^2 + i\omega\gamma_{Dis}} \quad (3)$$

which contains a Drude term, a broad resonance term, and a trion dissociation term. In this model, e is the elementary charge, m is the trion effective mass, n_F is the carrier concentration of free trions, n_B is the carrier concentration of trions that undergo the broad resonance response, n is the total trion concentration, and f is the oscillator strength of the trion dissociation so that $n \times f$ represents the concentration of trions dissociated. To calculate n_F , n_B , and $n \times f$, we set the trion effective mass to be $0.86 m_e$.⁴⁹ The trion effective mass was estimated as the sum of two hole effective masses and one electron effective mass.¹⁹ The results of our calculations are reported in Table 3 for the different absorbed fluences. In the last column of Table 3, we add n_F , n_B , and $n \times f$ to get the total trion concentration.

Looking at Table 3, we find that the total trion concentration n is roughly one-half of the absorbed fluence. To understand this, consider the process of trion formation

Table 2. Fitting Parameters for the Photoconductivity Curves in Figure 3

absorbed fluence [photons/cm ²]	C ₁ [S/s]	γ ₁ [THz]	ω ₀₁ [THz]	C ₂ [S/s]	γ ₂ [THz]	ω ₀₂ [THz]	C ₃ [S/s]	γ ₃ [THz]	ω ₀₃ [THz]
55 × 10 ¹²	6.0 × 10 ⁸	3.8	0	43 × 10 ⁸	31	3.2	23 × 10 ⁸	3.6	7.8
26 × 10 ¹²	2.6 × 10 ⁸	2.6	0	37 × 10 ⁸	42	3.3	10 × 10 ⁸	2.3	7.6
7.9 × 10 ¹²	0.7 × 10 ⁸	1.0	0	13 × 10 ⁸	53	3.2	1.0 × 10 ⁸	1.0	7.3

Table 3. Extracted Carrier Concentrations of Free Trions (n_F), Trions That Exhibit a Broad Resonance Response (n_B), and Trions That Are Dissociated (n × f) as a Function of Absorbed Fluence^a

absorbed fluence [photons/cm ²]	n _F [cm ⁻²]	n _B [cm ⁻²]	n × f [cm ⁻²]	n [cm ⁻²]
55 × 10 ¹²	1.8 × 10 ¹²	13 × 10 ¹²	7.0 × 10 ¹²	22 × 10 ¹²
26 × 10 ¹²	0.8 × 10 ¹²	11 × 10 ¹²	3.1 × 10 ¹²	15 × 10 ¹²
7.9 × 10 ¹²	0.2 × 10 ¹²	4.0 × 10 ¹²	0.3 × 10 ¹²	4.5 × 10 ¹²

^aThe last column gives the total trion concentration n by adding n_F , n_B , and $n \times f$.

described earlier. For a trion to form, an exciton and free charge must first be created. When pumping on resonance, an exciton is created when an electron in the valence band absorbs a photon and binds to a hole. Additionally, an electron in the valence band can absorb a photon and be excited into an immobile defect state, thus creating a free hole in the valence band. The exciton then captures this free hole to form a trion. From this analysis, we see that forming a single trion costs the price of two photons (one to create the exciton and one to create the free hole). Therefore, the total trion concentration n should be one-half of the absorbed fluence.

To understand the possible decay mechanisms of trions in monolayer WS₂, we fit the dynamics of the terahertz photoconductivity to a biexponential model. We find that the terahertz photoconductivity has two decay components: a short decay on the order of hundreds of femtoseconds and a longer decay on the order of picoseconds. In Figure 4, we

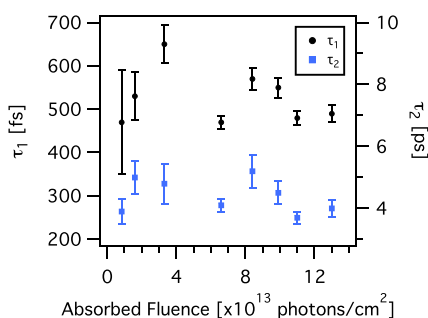


Figure 4. Fast (τ_1) (black circles) and slow (τ_2) (blue squares) time constants extracted from biexponential fits to the photoconductivity dynamics presented in Figure 1d as a function of absorbed fluence.

present the short and long decay constants as a function of absorbed fluence and find that both decay constants are fluence independent. In Table 4, we present the relative weights of the fast and slow decay components, in which we find that at low fluences the fast and slow decay components occur equally, while at higher fluences the fast decay component dominates. Given these observations, we tentatively assign the fast decay to trion–phonon scattering and the slow decay to defect-mediated trion dissociation. In the trion–phonon scattering mechanism, optical phonons that are created by the excitation pulse increase the temperature of the trions. The trions, as a result, have more kinetic energy and consequently shorter scattering times since they are moving faster. With shorter scattering times, the trions have lower mobility, therefore reducing the photoconductivity. Since optical phonons in monolayer WS₂ are expected to have a lifetime of ~ 1 ps as estimated from their Raman line widths,⁵⁰ the photoconductivity should decay within 1 ps as well, which is what we observe when measuring the fast decay in monolayer WS₂ (around 600 fs). The fact that the fast decay is stronger at higher fluences (Table 4) also indicates that trion–phonon scattering may be the mechanism for the fast decay component. This is because at higher fluences more optical phonons are created, thus making trion–phonon scattering the more dominant decay process. For the slow decay component of the photoconductivity, we think that trions decay through a defect-mediated process. Previous work has shown that trions in monolayer MoS₂ decay through defect-mediated processes.³⁵ In this kind of mechanism, an electron in a defect state recombines with one of the holes of the positive trion. This leaves behind an exciton, thus reducing the photoconductivity because excitons are not expected to directly contribute to the photoconductivity in the frequency range of our experiment. Since the trion density is on the order of the defect density, a fluence dependence on the slow decay constant is not expected, which agrees with our measurements (Figure 4). The fact that the NRL sample has a faster slow decay constant than the commercial sample (Figure 1b) also supports this idea that the slow decay mechanism is defect mediated. The NRL sample has more defects than the commercial sample, and thus, the trions should decay more quickly.

CONCLUSIONS

In summary, we observed a photoinduced increase in conductivity in monolayer WS₂ via broad-band time-resolved terahertz spectroscopy, which we attribute to ultrafast positive

Table 4. Relative Weights of the Fast and Slow Components of the Biexponential Fits to the Terahertz Photoconductivity Dynamics Presented in Figure 1d as a Function of Absorbed Fluence

	absorbed fluence [$\times 10^{13}$ photons/cm ²]							
	0.84	1.6	3.3	6.6	8.4	9.9	11	13
fast component	42%	51%	72%	71%	75%	74%	72%	73%
slow component	58%	49%	28%	29%	25%	26%	28%	27%

trion formation. We find that the frequency-dependent photoconductivity can be modeled as a sum of three components: a Drude component, a broad resonance component, and a dissociation component at the trion binding energy. This is the first direct measurement of the trion binding energy in the far-infrared in monolayer WS₂. Further analysis shows that trion formation is defect mediated, in which one trion forms for every two photons absorbed. This leads to a saturation in the photoresponse as the fluence reaches 4.8×10^{13} photons/cm². These results and analysis provide valuable insight into how trions behave in two-dimensional systems, and we think they will be useful in understanding the nonequilibrium carrier dynamics of other two-dimensional systems.

■ ASSOCIATED CONTENT

Supporting Information

The Supporting Information is available free of charge at <https://pubs.acs.org/doi/10.1021/acs.jpcc.9b08483>.

Figures illustrating typical terahertz waveforms and spectra, details concerning the measurement of the temperature-dependent absorption spectrum of monolayer WS₂, details about the calculation of the photoconductivity, and discussion on positive photoconductivity, trion mobilities, and photoconductivity resulting from above resonance pump excitation (PDF)

■ AUTHOR INFORMATION

Corresponding Authors

*E-mail: jgus1@umbc.edu.

*E-mail: hayden@umbc.edu.

ORCID

Jon K. Gustafson: 0000-0003-1745-3121

Paul D. Cunningham: 0000-0002-3602-1503

Kathleen M. McCreary: 0000-0003-2737-585X

Berend T. Jonker: 0000-0001-8816-7857

Notes

The authors declare no competing financial interest.

■ ACKNOWLEDGMENTS

J.K.G. acknowledges the support of the Department of Education through a GAANN Fellowship under award number P200A150003-17. P.D.C., K.M.M., and B.T.J. acknowledge support by the Office of Naval Research through core programs at the U.S. Naval Research Laboratory (NRL) and the NRL Nanoscience Institute.

■ REFERENCES

- (1) Yun, W. S.; Han, S. W.; Hong, S. C.; Kim, I. G.; Lee, J. D. Thickness and Strain Effects on Electronic Structures of Transition Metal Dichalcogenides: 2H-MX₂ Semiconductors (M = Mo, W; X = S, Se, Te). *Phys. Rev. B: Condens. Matter Mater. Phys.* **2012**, *85*, 033305.
- (2) Mak, K. F.; Lee, C.; Hone, J.; Shan, J.; Heinz, T. F. Atomically Thin MoS₂: A New Direct-Gap Semiconductor. *Phys. Rev. Lett.* **2010**, *105*, 136805.
- (3) Castellanos-Gomez, A. Why all the Fuss About 2D Semiconductors? *Nat. Photonics* **2016**, *10*, 202–204.
- (4) Xia, F. N.; Wang, H.; Xiao, D.; Dubey, M.; Ramasubramanian, A. Two-Dimensional Material Nanophotonics. *Nat. Photonics* **2014**, *8*, 899–907.

(5) Mak, K. F.; Shan, J. Photonics and Optoelectronics of 2D Semiconductor Transition Metal Dichalcogenides. *Nat. Photonics* **2016**, *10*, 216–226.

(6) Zhu, Z. Y.; Cheng, Y. C.; Schwingenschlogl, U. Giant Spin-Orbit-Induced Spin Splitting in Two-Dimensional Transition-Metal Dichalcogenide Semiconductors. *Phys. Rev. B: Condens. Matter Mater. Phys.* **2011**, *84*, 153402.

(7) Xiao, D.; Liu, G. B.; Feng, W. X.; Xu, X. D.; Yao, W. Coupled Spin and Valley Physics in Monolayers of MoS₂ and Other Group-VI Dichalcogenides. *Phys. Rev. Lett.* **2012**, *108*, 196802.

(8) Cao, T.; Wang, G.; Han, W. P.; Ye, H. Q.; Zhu, C. R.; Shi, J. R.; Niu, Q.; Tan, P. H.; Wang, E.; Liu, B. L.; Feng, J. Valley-Selective Circular Dichroism of Monolayer Molybdenum Disulfide. *Nat. Commun.* **2012**, *3*, 887.

(9) Mak, K. F.; He, K. L.; Shan, J.; Heinz, T. F. Control of Valley Polarization in Monolayer MoS₂ by Optical Helicity. *Nat. Nanotechnol.* **2012**, *7*, 494–498.

(10) Yao, W.; Xiao, D.; Niu, Q. Valley-Dependent Optoelectronics from Inversion Symmetry Breaking. *Phys. Rev. B: Condens. Matter Mater. Phys.* **2008**, *77*, 235406.

(11) Wang, G.; Chernikov, A.; Glazov, M. M.; Heinz, T. F.; Marie, X.; Amand, T.; Urbaszek, B. Colloquium: Excitons in Atomically Thin Transition Metal Dichalcogenides. *Rev. Mod. Phys.* **2018**, *90*, 021001.

(12) Chernikov, A.; Berkelbach, T. C.; Hill, H. M.; Rigosi, A.; Li, Y. L.; Aslan, O. B.; Reichman, D. R.; Hybertsen, M. S.; Heinz, T. F. Exciton Binding Energy and Nonhydrogenic Rydberg Series in Monolayer WS₂. *Phys. Rev. Lett.* **2014**, *113*, 076802.

(13) Ivchenko, E. L. *Optical Spectroscopy of Semiconductor Nanostructures*; Alpha Science International Ltd.: Harrow, U.K., 2005; pp 70–86.

(14) Berkelbach, T. C.; Hybertsen, M. S.; Reichman, D. R. Theory of Neutral and Charged Excitons in Monolayer Transition Metal Dichalcogenides. *Phys. Rev. B: Condens. Matter Mater. Phys.* **2013**, *88*, 045318.

(15) Hichri, A.; Ben Amara, I.; Ayari, S.; Jaziri, S. Dielectric Environment and/or Random Disorder Effects on Free, Charged and Localized Excitonic States in Monolayer WS₂. *J. Phys.: Condens. Matter* **2017**, *29*, 435305.

(16) Chakraborty, C.; Qiu, L. Y.; Konthasinghe, K.; Mukherjee, A.; Dhara, S.; Vamivakas, N. 3D Localized Trions in Monolayer WSe₂ in a Charge Tunable van der Waals Heterostructure. *Nano Lett.* **2018**, *18*, 2859–2863.

(17) Mitioglu, A. A.; Plochocka, P.; Jadcak, J. N.; Escoffier, W.; Rikken, G.; Kulyuk, L.; Maude, D. K. Optical Manipulation of the Exciton Charge State in Single-Layer Tungsten Disulfide. *Phys. Rev. B: Condens. Matter Mater. Phys.* **2013**, *88*, 245403.

(18) Mouri, S.; Miyauchi, Y.; Matsuda, K. Tunable Photoluminescence of Monolayer MoS₂ via Chemical Doping. *Nano Lett.* **2013**, *13*, 5944–5948.

(19) Peimyoo, N.; Yang, W. H.; Shang, J. Z.; Shen, X. N.; Wang, Y. L.; Yu, T. Chemically Driven Tunable Light Emission of Charged and Neutral Excitons in Monolayer WS₂. *ACS Nano* **2014**, *8*, 11320–11329.

(20) Plechinger, G.; Nagler, P.; Kraus, J.; Paradiso, N.; Strunk, C.; Schuller, C.; Korn, T. Identification of Excitons, Trions and Biexcitons in Single-Layer WS₂. *Phys. Status Solidi RRL* **2015**, *9*, 457–461.

(21) Ross, J. S.; Wu, S. F.; Yu, H. Y.; Ghimire, N. J.; Jones, A. M.; Aivazian, G.; Yan, J. Q.; Mandrus, D. G.; Xiao, D.; Yao, W.; Xu, X. D. Electrical Control of Neutral and Charged Excitons in a Monolayer Semiconductor. *Nat. Commun.* **2013**, *4*, 1474.

(22) Singh, A.; Moody, G.; Tran, K.; Scott, M. E.; Overbeck, V.; Berghauer, G.; Schaibley, J.; Seifert, E. J.; Pleskot, D.; Gabor, N. M.; Yan, J. Q.; Mandrus, D. G.; Richter, M.; Malic, E.; Xu, X. D.; Li, X. Q. Trion Formation Dynamics in Monolayer Transition Metal Dichalcogenides. *Phys. Rev. B: Condens. Matter Mater. Phys.* **2016**, *93*, 041401.

- (23) Mak, K. F.; He, K. L.; Lee, C.; Lee, G. H.; Hone, J.; Heinz, T. F.; Shan, J. Tightly Bound Trions in Monolayer MoS₂. *Nat. Mater.* **2013**, *12*, 207–211.
- (24) Paur, M.; Molina-Mendoza, A. J.; Bratschitsch, R.; Watanabe, K.; Taniguchi, T.; Mueller, T. Electroluminescence from Multi-Particle Exciton Complexes in Transition Metal Dichalcogenide Semiconductors. *Nat. Commun.* **2019**, *10*, 1709.
- (25) Katoch, J.; Ulstrup, S.; Koch, R. J.; Moser, S.; McCreary, K. M.; Singh, S.; Xu, J. S.; Jonker, B. T.; Kawakami, R. K.; Bostwick, A.; Rotenberg, E.; Jozwiak, C. Giant Spin-Splitting and Gap Renormalization Driven by Trions in Single-Layer WS₂/h-BN Heterostructures. *Nat. Phys.* **2018**, *14*, 355–359.
- (26) Hanbicki, A. T.; Kioseoglou, G.; Currie, M.; Hellberg, C. S.; McCreary, K. M.; Friedman, A. L.; Jonker, B. T. Anomalous Temperature-Dependent Spin-Valley Polarization in Monolayer WS₂. *Sci. Rep.* **2016**, *6*, 18885.
- (27) Ceballos, F.; Cui, Q. N.; Bellus, M. Z.; Zhao, H. Exciton Formation in Monolayer Transition Metal Dichalcogenides. *Nanoscale* **2016**, *8*, 11681–11688.
- (28) Cunningham, P. D.; Hanbicki, A. T.; McCreary, K. M.; Jonker, B. T. Photoinduced Bandgap Renormalization and Exciton Binding Energy Reduction in WS₂. *ACS Nano* **2017**, *11*, 12601–12608.
- (29) Docherty, C. J.; Parkinson, P.; Joyce, H. J.; Chiu, M. H.; Chen, C. H.; Lee, M. Y.; Li, L. J.; Herz, L. M.; Johnston, M. B. Ultrafast Transient Terahertz Conductivity of Monolayer MoS₂ and WSe₂ Grown by Chemical Vapor Deposition. *ACS Nano* **2014**, *8*, 11147–11153.
- (30) Chernikov, A.; Ruppert, C.; Hill, H. M.; Rigosi, A. F.; Heinz, T. F. Population Inversion and Giant Bandgap Renormalization in Atomically Thin WS₂ Layers. *Nat. Photonics* **2015**, *9*, 466–470.
- (31) Shi, H. Y.; Yan, R. S.; Bertolazzi, S.; Brivio, J.; Gao, B.; Kis, A.; Jena, D.; Xing, H. G.; Huang, L. B. Exciton Dynamics in Suspended Monolayer and Few-Layer MoS₂ 2D Crystals. *ACS Nano* **2013**, *7*, 1072–1080.
- (32) Cunningham, P. D.; McCreary, K. M.; Jonker, B. T. Auger Recombination in Chemical Vapor Deposition-Grown Monolayer WS₂. *J. Phys. Chem. Lett.* **2016**, *7*, 5242–5246.
- (33) Sun, D. Z.; Rao, Y.; Reider, G. A.; Chen, G. G.; You, Y. M.; Brezin, L.; Harutyunyan, A. R.; Heinz, T. F. Observation of Rapid Exciton-Exciton Annihilation in Monolayer Molybdenum Disulfide. *Nano Lett.* **2014**, *14*, 5625–5629.
- (34) Korn, T.; Heydrich, S.; Hirmer, M.; Schmutzler, J.; Schuller, C. Low-Temperature Photocarrier Dynamics in Monolayer MoS₂. *Appl. Phys. Lett.* **2011**, *99*, 102109.
- (35) Lui, C. H.; Frenzel, A. J.; Pilon, D. V.; Lee, Y. H.; Ling, X.; Akselrod, G. M.; Kong, J.; Gedik, N. Trion-Induced Negative Photoconductivity in Monolayer MoS₂. *Phys. Rev. Lett.* **2014**, *113*, 166801.
- (36) Xing, X.; Zhao, L. T.; Zhang, Z. Y.; Liu, X. K.; Zhang, K. L.; Yu, Y.; Lin, X.; Chen, H. Y.; Chen, J. Q.; Jin, Z. M.; Xu, J. H.; Ma, G. H. Role of Photoinduced Exciton in the Transient Terahertz Conductivity of Few-Layer WS₂ Laminate. *J. Phys. Chem. C* **2017**, *121*, 20451–20457.
- (37) Cunningham, P. D.; McCreary, K. M.; Hanbicki, A. T.; Currie, M.; Jonker, B. T.; Hayden, L. M. Charge Trapping and Exciton Dynamics in Large-Area CVD Grown MoS₂. *J. Phys. Chem. C* **2016**, *120*, 5819–5826.
- (38) Kar, S.; Su, Y.; Nair, R. R.; Sood, A. K. Probing Photoexcited Carriers in a Few-Layer MoS₂ Laminate by Time-Resolved Optical Pump-Terahertz Probe Spectroscopy. *ACS Nano* **2015**, *9*, 12004–12010.
- (39) McCreary, K. M.; Hanbicki, A. T.; Jernigan, G. G.; Culbertson, J. C.; Jonker, B. T. Synthesis of Large-Area WS₂ monolayers with Exceptional Photoluminescence. *Sci. Rep.* **2016**, *6*, 19159.
- (40) McCreary, K. M.; Hanbicki, A. T.; Singh, S.; Kawakami, R. K.; Jernigan, G. G.; Ishigami, M.; Ng, A.; Brintlinger, T. H.; Stroud, R. M.; Jonker, B. T. The Effect of Preparation Conditions on Raman and Photoluminescence of Monolayer WS₂. *Sci. Rep.* **2016**, *6*, 35154.
- (41) Cunningham, P. D.; Hayden, L. M.; Yip, H. L.; Jen, A. K. Y. Charge Carrier Dynamics in Metalated Polymers Investigated by Optical-Pump Terahertz-Probe Spectroscopy. *J. Phys. Chem. B* **2009**, *113*, 15427–15432.
- (42) Xie, X.; Dai, J. M.; Zhang, X. C. Coherent Control of THz Wave Generation in Ambient Air. *Phys. Rev. Lett.* **2006**, *96*, 075005.
- (43) Wu, Q.; Zhang, X. C. 7 Terahertz Broadband GaP Electro-Optic Sensor. *Appl. Phys. Lett.* **1997**, *70*, 1784–1786.
- (44) Chakkittakandy, R.; Corver, J.; Planken, P. C. M. Quasi-Near Field Terahertz Generation and Detection. *Opt. Express* **2008**, *16*, 12794–12805.
- (45) Carozo, V.; Wang, Y. X.; Fujisawa, K.; Carvalho, B. R.; McCreary, A.; Feng, S. M.; Lin, Z.; Zhou, C. J.; Perea-Lopez, N.; Elias, A. L.; Kabius, B.; Crespi, V. H.; Terrones, M. Optical Identification of Sulfur Vacancies: Bound Excitons at the Edges of Monolayer Tungsten Disulfide. *Sci. Adv.* **2017**, *3*, e1602813.
- (46) Salehi, S.; Saffarzadeh, A. Optoelectronic Properties of Defective MoS₂ and WS₂ Monolayers. *J. Phys. Chem. Solids* **2018**, *121*, 172–176.
- (47) Rosenberger, M. R.; Chuang, H. J.; McCreary, K. M.; Li, C. H.; Jonker, B. T. Electrical Characterization of Discrete Defects and Impact of Defect Density on Photoluminescence in Monolayer WS₂. *ACS Nano* **2018**, *12*, 1793–1800.
- (48) Kastl, C.; Koch, R. J.; Chen, C. T.; Eichhorn, J.; Ulstrup, S.; Bostwick, A.; Jozwiak, C.; Kuykendall, T. R.; Borys, N. J.; Toma, F. M.; Aloni, S.; Weber-Bargioni, A.; Rotenberg, E.; Schwartzberg, A. M. Effects of Defects on Band Structure and Excitons in WS₂ Revealed by Nanoscale Photoemission Spectroscopy. *ACS Nano* **2019**, *13*, 1284–1291.
- (49) Thilagam, A. Exciton Complexes in Low Dimensional Transition Metal Dichalcogenides. *J. Appl. Phys.* **2014**, *116*, 053523.
- (50) Lee, Y. H.; Yu, L. L.; Wang, H.; Fang, W. J.; Ling, X.; Shi, Y. M.; Lin, C. T.; Huang, J. K.; Chang, M. T.; Chang, C. S.; Dresselhaus, M.; Palacios, T.; Li, L. J.; Kong, J. Synthesis and Transfer of Single-Layer Transition Metal Disulfides on Diverse Surfaces. *Nano Lett.* **2013**, *13*, 1852–1857.